https://doi.org/10.5194/egusphere-2023-1494
Preprint. Discussion started: 11 September 2023

Effects of longwave radiative cooling on advection fog over the Northwest Pacific Ocean: Observations and large eddy simulations

Liu Yang[1], Saisai Ding[2], Jing-Wu Liu[2*], Su-Ping Zhang[2]

[1]College of Aviation Meteorology, Civil Aviation Flight University of China, Guanghan, China

[2] Frontier Science Center for Deep Ocean Multispheres and Earth System (FDOMES), Physical Oceanography Laboratory, and Ocean–Atmosphere Interaction and Climate Laboratory, Ocean University of China, Qingdao, China

[*] Corresponding author: Jing-Wu Liu, Ocean University of China, 238 Songling Road, Qingdao, 266100, P. R. China

Email: liujingwu@126.com; liujingwu@ouc.edu.cn

https://doi.org/10.5194/egusphere-2023-1494
Preprint. Discussion started: 11 September 2023

Abstract

During the boreal summer, the prevailing southerlies traverse the sharp sea surface temperature (SST) front in the Northwest Pacific (NWP) Ocean, creating a stable air-sea interface characterized by surface air temperature (SAT) higher than SST, which promotes the frequent occurrence of advection fog. However, long-term shipborne observations reveal that during episodes of advection fog, SAT usually decreases below SST, with a peak relative frequency (~34.5%) to all fog observations before sunrise and a minimum relative frequency (~18.8%) before sunset. From a Lagrangian perspective, this study employs a turbulence-closure large-eddy simulation (LES) model to trace a fog column across the SST front and investigates how SAT drops below the SST during an advection fog event. The LES model, incorporating constant solar radiation, successfully simulates the evolution of advection fog and the negative SAT-SST. Simulation results show that once the near-surface air condenses, the thermal turbulence is generated by strong longwave radiation cooling (LWC) at the fog top. The influence of LWC on the fog layer surpasses the cooling effect of the near-surface mechanical turbulence ~2 hours after the fog formation, while the fog column is still positioned over the SST front. When the fog column arrives the cold flank of the SST front, the top-down developing mixed layer induced by the LWC reaches the surface, causing the SAT to drop below SST. The LES model with diurnal solar radiation well simulates the diurnal variation in SAT-SST during the fog event, suggesting that the model captures the essential processes responsible for negative SAT-SST. This study highlights the significance of fog-top cooling and its associated thermal turbulence in the evolution of advection fog. Given the challenges faced by numerical weather prediction models in forecasting sea fog, our findings suggest that observations of negative SAT-SST during advection fog episodes present an opportunity to enhance the performance of these models in simulating the thermal turbulence induced by the LWC at the fog top.

https://doi.org/10.5194/egusphere-2023-1494
Preprint. Discussion started: 11 September 2023

1. Introduction

The northwest Pacific Ocean experiences heavy sea fog during summer (Wang, 1985; Koračin and Dorman, 2017), which is of great importance due to its significant impact on maritime activities (Gultepe et al., 2007; Trémant, 1987). However, present numerical weather prediction models struggle to accurately forecast sea fog (Gao et al., 2007), partly because their coarse resolutions inadequately resolve boundary-layer processes within the thin fog layer with depths of hundreds of meters (Yang et al., 2019). Therefore, enhancing our understanding of turbulent boundary-layer processes becomes imperative for refining the accuracy of sea fog predictions.

The sea surface temperature (SST) gradient related to the Kuroshio Extension often triggers advection fog under summertime warm advection (Wang, 1985; Koračin and Dorman, 2017). The prevailing southerlies on the western flank of the subtropical high transport warm, humid air across the Kuroshio Extension front (Zhang et al., 2014; Long et al., 2016; Koracin and Dorman, 2017). The abrupt decline in SST effectively cools the near-surface humid air through mechanical turbulence, resulting in air saturation and fog formation (Taylor, 1917; Rodhe, 1962; Lewis et al., 2004; Gao et al., 2007; Yang et al., 2020). However, the near-surface cooling induced by mechanical turbulence appears to be important in the initial phase of advection fog (Hu et al., 2006).

Once fog forms, the longwave radiation cooling (LWC) effect at the fog top commences to influence fog evolution. Earlier observational studies conjectured that the LWC at the fog top plays an important role in the fog's development and maintenance (Douglas, 1930; Lamb, 1943; Petterssen, 1938; Findlater et al., 1989). The LWC at the fog top induces negative buoyancy and thermal turbulence (Bretherton and Wyant, 1997; Gerber et al., 2005, 2013; Guan et al., 1997; Yamaguchi and Randall, 2008; Koračin and Dorman, 2017). This thermal turbulence further promotes vertical mixing and cools the fog layer (Rogers and Koračin, 1992; Koracin et al., 2001, 2005; Yang et al., 2018). Huang et al. (2015) identified a so-called thermal turbulence interface, which separates the thermal turbulence induced by the fog-top LWC and near-surface mechanical turbulence. Despite previous studies recognizing the significance of the LWC at the fog top, its relative importance to the near-surface cooling by the mechanical turbulence remains to be determined.

Observational evidence underscores the significance of the LWC at fog top, as surface air temperature (SAT) occasionally falls below SST during advection fog episodes. This means that the sea surface acts to heat the fog layer (referred to as sea fog with sea surface heating [ssH] hereafter). Instances of ssH fog have been reported in advection fog events over the Yellow Sea (Zhang et al., 2012; Zhang and Ren, 2010), during the haar peak over the North Sea (Lamb et al., 1943), and in the fog off the California coast (Leipper, 1948, 1994), as well as off the northeastern coast of Scotland (Findlater et al. 1989). Based on long-term buoy observations, Yang et al. (2018) found that the relative frequency of ssH fog to advection fog reaches up to ~30% over the Yellow Sea in summer. Their composite analysis revealed that ssH fog is associated with stronger atmospheric subsidence, a drier free atmosphere, and sharper capping inversions, indicative of a crucial role of the fog-top LWC for ssH fog. However, limited observations of the boundary-layer vertical structure over the sea inhibit the understanding of how fog-top LWC influences advection fog and leads to a negative SAT-SST.

In comparison to numerical weather prediction models, large eddy simulations (LES) with higher resolutions are capable of explicitly resolving larger thermal turbulent eddies within the boundary layer. LES has been successfully employed in studies related to clouds (Bretherton and Wyant, 1997; Wyant et al., 1997; Stevens 2000, 2007; Savic-Jovci and Stevens, 2008; McGibbon and Bretherton, 2017) and continental fog (Nakanishi, 2000; Bergot, 2013, 2016; Mazoyer et al. 2016; Maronga and Bosveld 2017; Schwenkel and Maronga 2019). Recently, the application of LES has extended to sea fog (Yang et al., 2021; Wainwright and Richter, 2021). Yang et al. (2021) used the climatological subsidence to force a LES model to study an advection fog event over the NWP. They found that the fog-top thermal turbulence induced by the LWC entrains the drier free atmospheric air into the boundary layer, which evaporates near-surface fog droplets, leading to a transition of fog into stratus. This simulated fog-to-stratus transition based on LES is consistent with that in long-term observations.

https://doi.org/10.5194/egusphere-2023-1494
Preprint. Discussion started: 11 September 2023

Wainwright and Richter (2021) attempted to use LES to examine the sensitivity of sea fog to the cloud-droplet number concentration, turbulent mixing, and SAT-SST.

The present study primarily focuses on the ssH fog during advection fog episodes. We first analyze the statistical features of the ssH fog over the NWP using long-term shipborne observations. ssH fog was observed during the advection fog episode studied by Yang et al. (2021). Thus, this study extends the LES simulation conducted by Yang et al. (2021) by forcing the LES with more realistic free-atmospheric subsidence to specifically investigate the boundary-layer processes responsible for ssH fog. We quantify the heat budgets of the fog layer based on the LES results to compare the effects of fog-top LWC and near-surface cooling and identify the interface between the thermal and mechanical turbulence. The results highlight the importance of the fog-top cooling and its induced thermal turbulence on the evolution of advection fog.

The paper is organized as follows. Section 2 describes the data sets and methods used in this study. Section 3 analyzes the observational characteristics of sea fog with ssH over the NWP. Section 4 presents the simulation results obtained using constant solar radiation and diurnal cycle radiation. Section 5 provides a summary and discussions.

2. Data and method

2.1 ICOADS and ERA5

We use shipborne observations provided by the International Comprehensive Ocean–Atmosphere Data Set (ICOADS) to investigate the occurrence of sea fog over the summer NWP. Fog is identified when the present-weather code is between 10 and 12 or between 40 and 49, and the visibility is lower than 1 km (Bari et al., 2016; Yang et al., 2021). In addition, we also use the SST, SAT, and 10 m winds to examine the sea-air interface conditions during sea fog. We include ~6×10^4 fog reports over the NWP between 1998 and 2018 to explore the sea fog climatologies and select a fog case that took place during 1- 4 July 2013 for further analysis and simulation.

To construct the idealized initial conditions for the sea fog simulation, we use the

https://doi.org/10.5194/egusphere-2023-1494
Preprint. Discussion started: 11 September 2023

fifth generation of the European Centre for Medium-Range Weather Forecasts atmospheric reanalysis (ERA5, Hersbach et al., 2020). ERA5 fields are on a 0.25° × 0.25° grid with 16 levels below 500 hPa.

2.2 UCLA-LES model

UCLA-LES is a three-dimensional, turbulence-closure boundary layer model, which has prognostic variables such as total water mixing ratio q_t, liquid water potential temperature θ_l, three components of wind, and turbulent fluxes. This model is often used to simulate stable, neutral, and convective boundary layers (Stevens et al., 2005).

The parameterization for subgrid fluxes in UCLA-LES is based on the Smagorinsky–Lilly model (Smagorinsky, 1963; Lilly, 1967) to satisfy the model closure. This model can explicitly compute the thermal turbulent flux and appropriately describe the turbulent mixing process within the boundary layer (Stevens et al., 2005; Jiang et al., 2006). The radiative transfer is calculated by the δ-four-stream method (Fu and Liou, 1993; Pincus and Stevens, 2009). The radiative fluxes are calculated based on the background profiles of pressure, temperature, humidity, and ozone content (Stevens et al., 2003). The model has a warm-rain microphysical scheme (Seifert and Beheng, 2001) that assumes that cloud droplets are in equilibrium at a fixed concentration. The microphysics process is expressed by including the interaction within the same type and between different types of cloud and raindrops. We set a specified 100×10^6 g kg^{-1} cloud-droplet mixing ratio in our simulations.

2.3 Diagnostic equations

We analyze the budget of domain-averaged heat and water vapor to investigate the related physical processes responsible for sea fog evolution. The heat budget is calculated using

$$\frac{\partial \bar{\theta}}{\partial t} = -\frac{\partial \overline{w'\theta'}}{\partial z} - \frac{L_v E}{\bar{\rho} C_p} - \frac{1}{\bar{\rho} C_p}\frac{\partial \bar{Q}}{\partial z}, \quad (1)$$

where θ is potential temperature. The term on the right-hand side (RHS) describes the heat change from turbulent mixing, latent heat releasing, and the radiation effect. $\overline{w'\theta'}$ is the sum of resolved and sub-scale parameterized turbulent heat flux. L_v is the latent heat release of condensation or evaporation. ρ is air density. C_p = 1004.67 J kg^{-1} K^{-1} is

https://doi.org/10.5194/egusphere-2023-1494
Preprint. Discussion started: 11 September 2023

specific heat of moist air. Q is radiation flux. The water vapor budget equation is

$$\frac{\partial \overline{q_v}}{\partial t} = -\frac{\partial \overline{w' q_v'}}{\partial z} - \frac{E}{\overline{\rho}}, \tag{2}$$

where q_v is water vapor mixing ratio. The terms on the RHS describe the q_v change from turbulent mixing effect and evaporation/condensation. $\overline{w' q_v'}$ is the sum of resolved and sub-scale turbulent water vapor flux.

To diagnose the turbulent mixing process responsible for heat and moist variation, we compute the turbulent kinetic energy (TKE) budget using

$$\frac{\partial \overline{TKE}}{\partial t} = +\frac{g}{\theta_v}\left(\overline{u_i' \theta_v'}\right) - \overline{u_i' u_3'}\frac{\partial \overline{u_i}}{\partial x_3} - \frac{\partial\left(\overline{u_3' TKE}\right)}{\partial x_3} - \varepsilon, \tag{3}$$

where subscripts i = 1, 2, and 3 represent x, y, and z coordinates. The four terms on the RHS represent buoyancy production, mechanical production from wind shear, the vertical transport of TKE, and TKE dissipation due to friction, respectively.

3. Advection fog with ssH in ICOADS observations

3.1 Statistical features of ssH fog

To isolate advection fog, we trace back each ICOADS fog observation for 48 hours, using the 6-hourly horizontal wind fields ERA5 at 10 m. Our analysis includes 43,105 fog observations originating from warmer waters during the period of 1998-2018. Figure 1 shows the climatological frequency of advection fog, fog with sea surface cooling (ssC, SAT-SST > 0), and fog with ssH over the NWP during June-July-August (JJA). Advection fog is frequently observed on the cold flank of the Kuroshio Extension front, with a peak frequency of ~30% near the Kuril Islands, where intense tidal mixing results in SSTs below 10°C (Fig. 1a; Tokinaga and Xie, 2009). Advection fog with ssC primarily appears in a band-shaped region between 40°N and 52°N, a distribution similar to that of all advection fog (Fig. 1a, b). The frequency of ssH fog also peaks at ~10% near the Kuril Islands (Fig. 1c), but its region of maximal occurrence extends further downstream to the north of 52°N. A detailed comparison of Figs. 1a and 1b suggests that approximately half of the ssC fog transitions into ssH fog as the fog column migrates northward under prevailing southwesterlies.

https://doi.org/10.5194/egusphere-2023-1494
Preprint. Discussion started: 11 September 2023

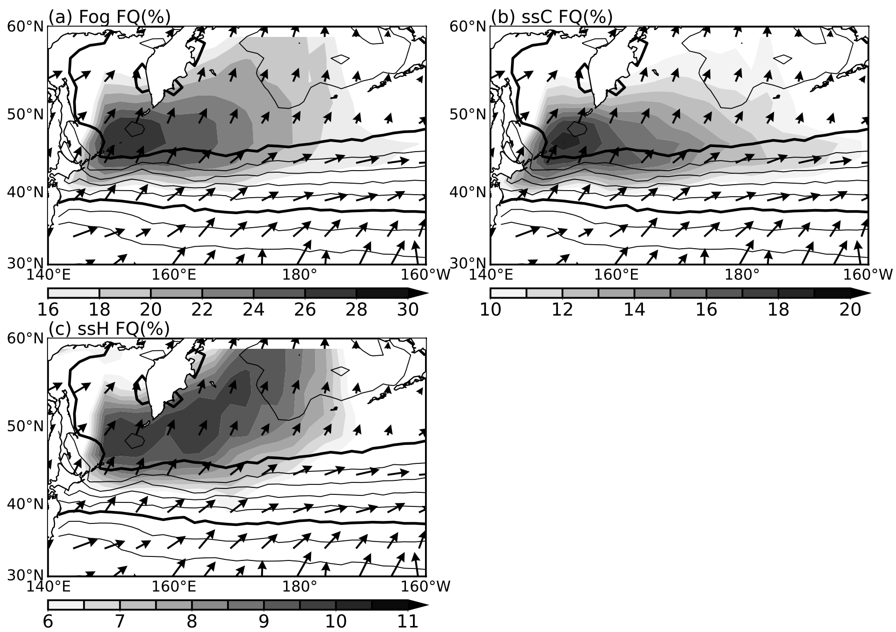

FIG. 1 Climatological SST (contours with 2-K intervals), surface winds (vectors, m s^{-1}), and frequencies (shading, %) of fog with (a) ssC and (b) ssH during June-July-August for 1998-2018. 283 K and 293 K SST contours are thickened. The SST and winds are based on ERA5, and the fog frequencies are obtained from ICOADS.

Figure 2 illustrates the probability density function (PDF) of the simultaneous SAT-SST values concurrent with advection fog over the NWP during JJA. The majority of these SAT-SST values exceed 0 °C (Fig. 2), which is consistent with the observational results of Fu and Song (2014). However, a substantial proportion (~27.5%) of advection fog in the NWP is associated with ssH fog. Based on coastal buoy observations, Yang et al. (2019) reported that ~30% of SAT falls below SST during fog events in the Yellow Sea. Li et al. (2022) also observed ~32% fog is with ssH over the northeast Pacific during winter. The consistent observations of advection fog with ssH imply that cooling mechanisms other than near-surface turbulent cooling have a substantial impact on the evolution of advection fog.

https://doi.org/10.5194/egusphere-2023-1494
Preprint. Discussion started: 11 September 2023

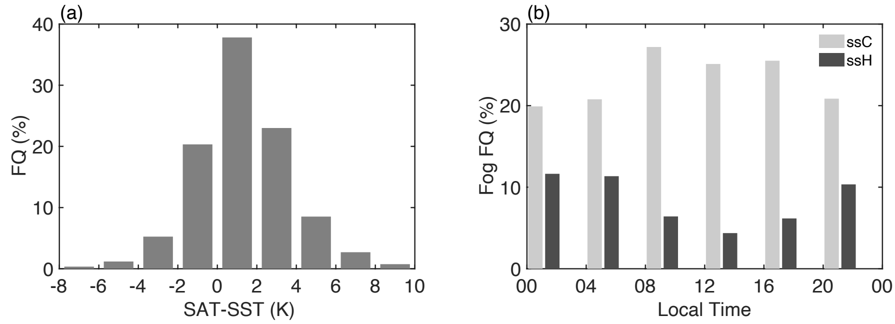

FIG. 2 (a) Probability density function (%) of SAT-SST (°C) concurrent with fog observations over the NWP (30-60°N, 140-200°E) during June-July-August based on ICOADS. (b) The frequencies of fog with ssH (dark grey bars) and ssC (light grey) as functions of local time.

There is a noticeable diurnal variation in ssH fog over the NWP (dark grey bars in Fig. 2b). Local time is determined based on the universal time of fog observations and their respective longitudes. The frequency of ssH fog reaches its maximum (~11.5%) and minimum (~4%) during 0000-0400 and 1200-1600 local time, respectively (the dark grey bars in Fig. 2b). Relative to all advection fog occurrences, the frequency of ssH fog is ~18.8% during the daytime and increases to ~34.5% at night. In contrast, the frequency of ssC fog is highest around sunrise (the light grey bars in Fig. 2b) and does not exhibit a clear diurnal variation. The evident diurnal cycle of ssH fog over the open sea is new to our knowledge and suggests that the radiative balance over fog top significantly alters the evolution of advection fog.

3.2 An ssH fog case

We examine the advection fog event during 01- 04 July 2013 over the NWP. The synoptic steady southwesterlies over the SST front caused the fog event (Fig. 4), and ICOADS observations reported no precipitation during this period. Further information regarding this fog event can be found in Yang et al. (2021). Our primary focus is on the negative SAT-SST observations during this fog episode (Fig. 4). Fog was first reported near the Kuril Islands at the night of 30 June (red stars in Figs. 2b), concurring with positive SAT-SST. The southwesterly winds, along with positive SAT-SST, signify the event as advection fog. As the saturated air moved northeastward, negative SAT-SST was detected within the fog patch during 02-04 July (blue stars in Figs. 4e-h). Notably, most of the ssH fog occurred at night.

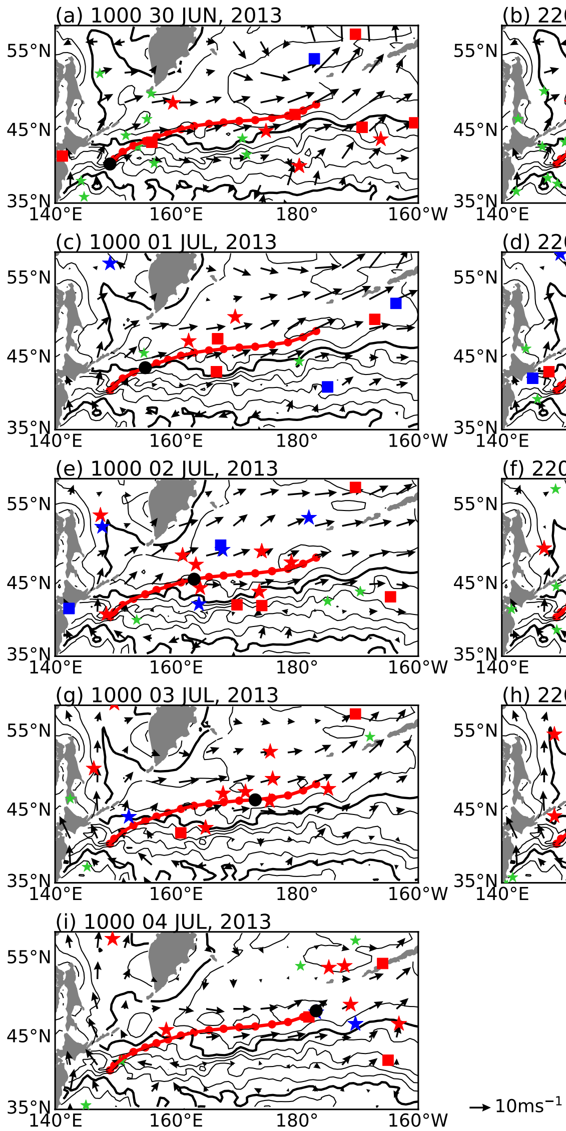

FIG. 4 ICOADS observations of the advection fog event during 30 June - 03 July, 2013. The blue and red stars represent ssH and ssC fog, respectively, and squares indicate stratus, and green stars indicate other cloud types or clear sky. The ICOADS observations and ERA5 10-m winds near 1000 LST from 30 June to 04 July are shown in (a), (c), (e), (g), and (i), respectively. The ICOADS reports and ERA5 winds between 2200-0800 (+1 day) LST are shown in (b), (d), (f), (h), respectively, to include more nighttime observations. The thick red line in each panel demonstrates the 4-day back trajectory from the ssH fog observation at 49.6°N 183.2°E, and the red dots are the location of the trajectory every 6 hours, and larger black dot indicating the location at the corresponding time of the panel. The contours are averaged ERA5 SST during 30 June-03 July, and the thick contours indicate 293 and 303 K, respectively.

https://doi.org/10.5194/egusphere-2023-1494
Preprint. Discussion started: 11 September 2023

4 Simulation with constant solar radiation

The synoptic processes associated with the fog event detailed in subsection 3b align closely with the climatological characteristics of ssH and ssC fog (Figs. 1 and 2). To uncover the boundary-layer processes responsible for the ssH fog, we use the UCLA-LES model to simulate this typical fog event from a Lagrangian perspective. We trace back an ssH fog observation at 49.6 °N 183.2 °E in Fig. 4i, which had an SAT-SST value of -1.2 °C. The air column consecutively experienced no fog, ssC, and ssH fog along the trajectory from 30 June to 04 July, 2013 (Fig. 4). The simplified SST along the trajectory and the simulation setups are the same as those in Yang et al. (2021), except for the divergence forcing in the free-atmosphere. Here, we apply a realistic divergence of 2×10^{-6} s^{-1}, which is double the climatological value in Yang et al. (2021). We first perform a simulation with fixed solar radiation.

4.1 Evolution in boundary-layer structure

Figure 5a depicts the time-height section of the liquid water mixing ratio (q_l) and virtual potential temperature (θ_v) for the air column in the simulation with constant solar radiation. We exclude the first 2 hours of results due to the model's spin-up. Liquid water initially appears near the surface (~20 m) at 0400 local standard time (LST) 01 July and rapidly extends to the surface within 1 h, resulting in fog formation. We define fog when q_l exceeds 0.02 g kg^{-1} (Kunkel, 1984). The fog persists until 1300 LST on 3 July, transitioning into stratus as the near-surface droplets evaporate. This transition results from the entrainment of the free-atmospheric dry air caused by the fog-top LWC (Yang et al., 2021). The height of the fog top grows rapidly from 20 to 330 m until 1000 LST 02 July and rarely varies thereafter. The capping inversion intensifies from 5 to 12 K after fog formation (Fig. 5a).

https://doi.org/10.5194/egusphere-2023-1494
Preprint. Discussion started: 11 September 2023

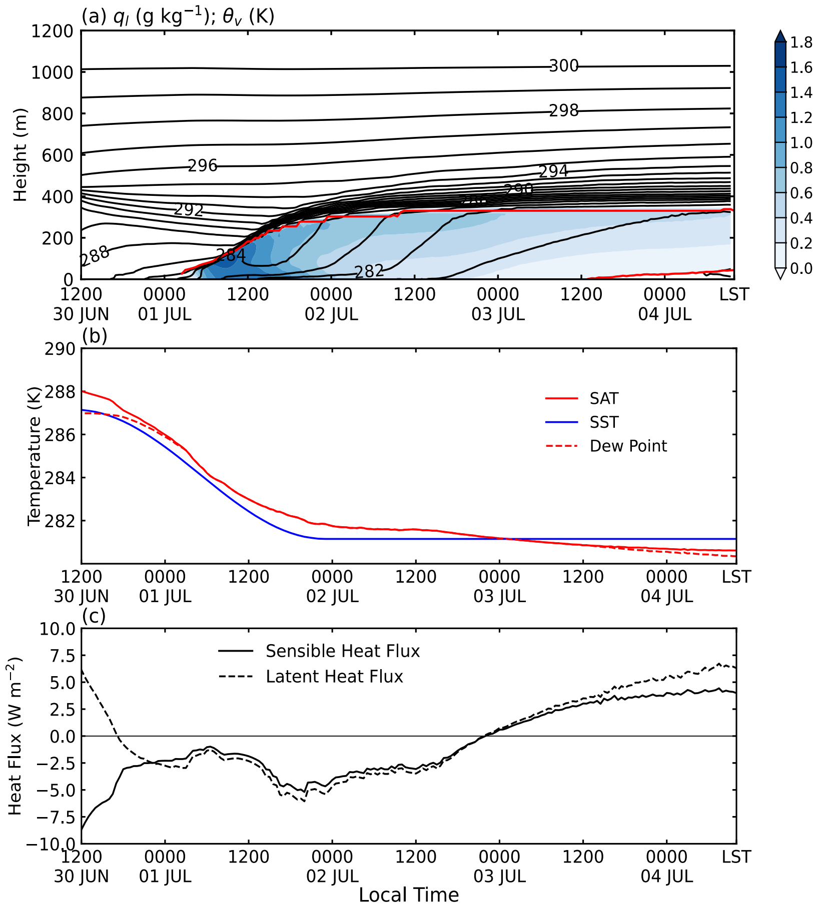

FIG. 5. (a) Time-height section of simulated liquid water mixing ratio (shading, g kg^{-1}), virtual potential temperature (contours, K) for constant solar radiation simulation. Red lines indicate the fog/cloud top and bottom, respectively. (b) SAT (red line, K), SST (blue, K) and surface dewpoint temperature (dashed red, K). (c) Same as (b) but for surface sensible heat flux (solid, W m^{-2}) and latent heat flux (dashed, W m^{-2}). Upward sensible and latent heat fluxes are positive.

The model successfully reproduces the ssH fog. Over the SST front, SAT follows the underlying SST with a difference of 0.8 K, resulting in strong downward sensible heat flux between -10 and -2 W m^{-2} (Figs. 5b and 5c). At 0500 LST on 01 July, SAT drops to the dewpoint at 285.6 K. After crossing the SST front, SAT is almost constant during the period of 0000-1200 LST on 02 July but quickly decreases afterward, falling below SST at 0000 LST on 03 July. From this time, both sensible and latent heat fluxes change their directions, indicating that the ocean begins to heat and moisten the surface air (Figs. 5b and 5c). The ssH fog sustains for 12 hours.

https://doi.org/10.5194/egusphere-2023-1494
Preprint. Discussion started: 11 September 2023

We divide the simulation into four phases: fog formation (from 1200 LST on 30 June to 0500 LST on 01 July) and development (from 0500 LST on 01 July to 0000 LST on 02 July) over the SST front, followed by fog maintenance with ssC (from 0000 LST on 02 July to 0000 LST on 03 July) and ssH (from 0000 to 1200 LST on 03 July) to the north of the SST front. Figure 6 shows boundary layer structure for the above four phases. The soundings of θ_v, total water mixing ratio (q_t), and q_l are domain-averaged and 2 h-averaged, centered at the selected times.

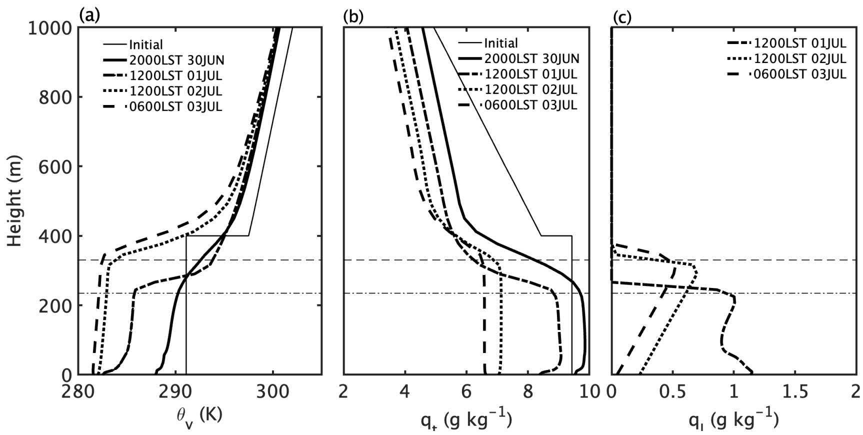

FIG. 6. Horizontal mean soundings for constant solar radiation simulation at 1000 LST on 30 June (thin solid line), 2000 LST on 30 June (solid), 1200 on LST 01 July (dot-dashed), 1200 LST on 02 July (dot) and 0600 LST on 03 July (dashed). (a) Virtual potential temperature (K), (b) total water mixing ratio (g kg^{-1}) and (c) liquid water mixing ratio (g kg^{-1}). Horizontal dot-dahsed line represents fog top height at 1200 on 01 July, and the horizontal dashed line represents fog top heights at 1200 on 02 July and 0600 on 03 July.

Before the fog formation, the cold sea surface efficiently cools the near-surface air, creating a stable boundary layer (Figs. 5a and 6a). q_t increases with height below 20 m and remains nearly constant within the boundary layer (Fig. 6b). The upward decrease in air temperature and increase in q_t result in the maximal relative humidity and saturation occurring near 20 m (Fig. 6a). Once fog forms, a mixed layer develops downward from the fog top to 50 m, capping the original stable layer produced by the cold sea surface (Fig. 6a). θ_v and q_t of the boundary layer decrease by ~6 K and ~1.5 g kg^{-1}, respectively, from 2000 LST on 30 June to 1200 LST on 01 July (Figs. 6a and 6b). q_l peaks near the surface and at fog top, respectively, and decreases with height within the stable layer below 50 m (Fig. 6c). The stratifications of θ_v, q_t and q_l indicate a

https://doi.org/10.5194/egusphere-2023-1494
Preprint. Discussion started: 11 September 2023

different cooling mechanism at the fog top from that at its bottom (Fig. 6a).

During the ssC fog phase, a well-mixed boundary layer develops, and θ_v decreases by 2 K from 1200 LST on 01 July to 1200 LST on 02 July (Figs. 6a and 6b). q_l peaks near the fog top (Fig. 6c). During the ssH fog phase, the sea surface heats and moistens the fog layer (Fig. 5b), while the fog layer keeps cooling and drying at a much slower rate (Fig. 6a), indicating that the LWC effect at the fog top dominates the fog cooling and maintenance. The thermal and moisture stratifications of ssH fog share a similar structure to those of ssC fog but with a deeper well-mixed layer (the long dashed lines in Fig. 6).

4.2 Heat and moist budgets

Figure 7 shows the profiles of heat and water vapor budgets at different phases. Figures 8a and 8b show the time series of surface heat and water vapor budget terms, respectively. Over the SST front, the turbulent mixing and longwave radiation effects cool the air near the surface and within the whole boundary layer due to the SST decrease (Figs. 7a and 8a). Fog forms due to the cooling of the air near the surface (Fig. 7a).

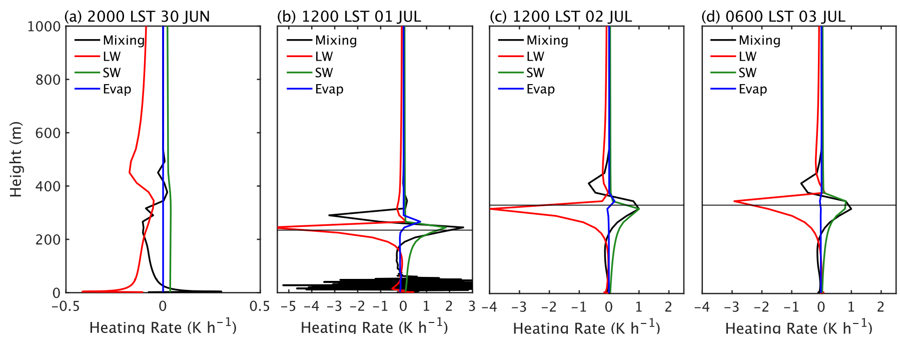

FIG. 7 Profiles of horizontal mean budget terms for heat (K h^{-1}) at (a) 2000 LST on 30, (b) 1200 LST on 01 July, (c) 1200 on 02 July and (d) 0600 LST on 03 July in the constant solar radiation simulation. The horizontal lines indicate fog/cloud top.

After the fog formation, the surface turbulent cooling intensifies dramatically, peaking at -1.35 K h^{-1}, leading to a marked decrease in SAT (Fig. 8a). The rapid growth of q_l releases latent heat through condensation, which partly offsets the cooling effect from turbulent mixing. Turbulent mixing keeps drying the surface air except for a brief period around 0900 on 1 June (Fig. 8b). Within the boundary layer, the longwave

https://doi.org/10.5194/egusphere-2023-1494
Preprint. Discussion started: 11 September 2023

radiation effect induces strong cooling at the fog top, and the resultant turbulent mixing cools the upper boundary layer (the red line in Fig. 7b). Additionally, the thermal turbulence helps entrain the warm, dry air from the free atmosphere, warming the air at the fog top while cooling the air above the fog layer (the black line in Fig. 7b).

When the fog volume moves north of the SST front (0000 LST on 02 July onward), the surface cooling and drying effects become weak due to the fixed SST (Fig. 8). However, the strong LWC persists at the fog top, inducing turbulent mixing that cools the entire fog layer (Figs. 6a and 7c). In this case, the effect of the fog-top LWC overcomes the surface cooling effect, causing SAT to drop below the SST. During the ssH phase, the LWC at the fog top slightly weakens and dominates the turbulent mixing cooling within the fog layer, causing the SAT to continuously decrease (Figs. 5b and 7d).

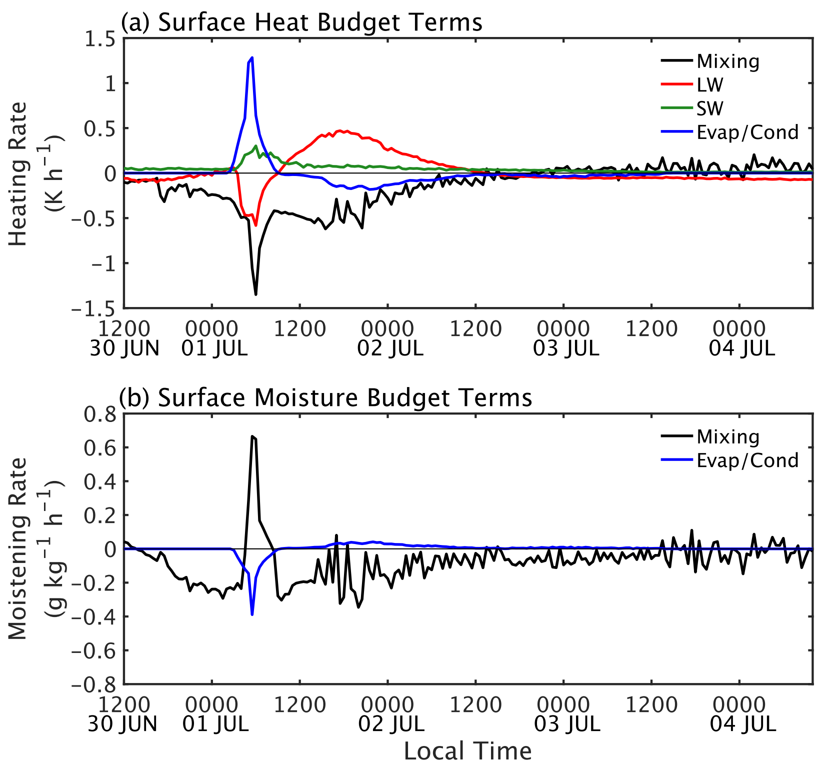

FIG. 8 Time series of horizontal mean budget terms at the surface for the constant solar radiation simulation: (a) heat (K h^{-1}) and (b) water vapor (g kg^{-1} h^{-1}).

https://doi.org/10.5194/egusphere-2023-1494
Preprint. Discussion started: 11 September 2023

We quantify the heat budget for the integral fog layer (Fig. 9). We determine the turbulent mixing term by calculating the difference between the turbulent heat fluxes at the surface and fog top, representing the surface sensible heat transport and the effect of the fog-top entrainment, respectively (the black and grey lines in Fig. 9). Prior to fog formation, the surface sensible heat transport drives the boundary layer cooling (the black line in Fig. 9). After the fog forms, the effect of longwave radiation acts to cool the boundary layer due to the longwave heat loss at fog top (the red line). The LWC effect rapidly exceeds surface cooling 2 hours after fog formation. Both shortwave radiation and entrainment at the fog top warm the fog layer, partially offsetting the effects of surface cooling and LWC. As the fog moves to the cold flank of the SST front, the surface cooling weakens and reverses, slightly heating the fog layer after the SAT drops below the SST. Overall, the persistent and strong LWC at the fog top dominates the fog evolution, resulting in the ssH fog.

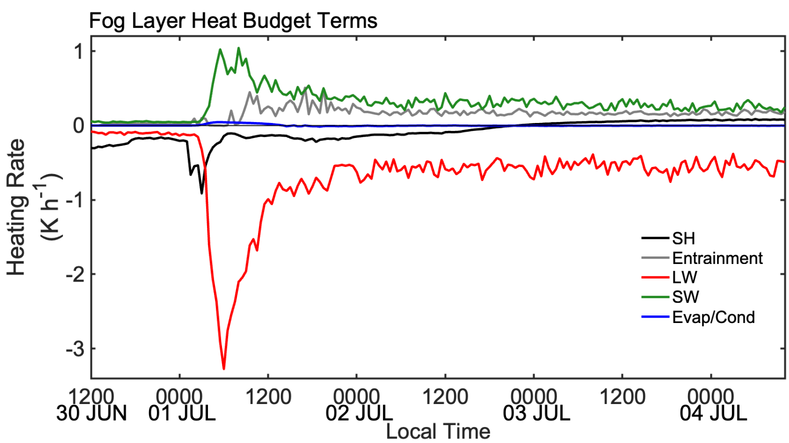

FIG. 9 Time series of horizontal mean heat budget terms (K h^{-1}) of the integral boundary layer for the constant solar radiation simulation.

4.3 TKE and its budget

Figure 10a presents the time-height cross section of TKE for the simulation with constant solar radiation. Prior to the fog formation (0400 LST on 01 July), TKE exhibits a relatively low magnitude below 200 m (Fig. 10a), produced by the near-surface wind shear and dissipated by friction and buoyancy (Fig. 11a). Mechanical turbulence facilitates the transport of cooling from the surface, contributing to the fog formation. Following the fog formation, the LWC at the fog top induces buoyancy production of

https://doi.org/10.5194/egusphere-2023-1494
Preprint. Discussion started: 11 September 2023

turbulence over the upper boundary layer (Fig. 11b), leading to a noticeable peak in TKE near the fog top ~10 hours after its formation (Fig. 10a).

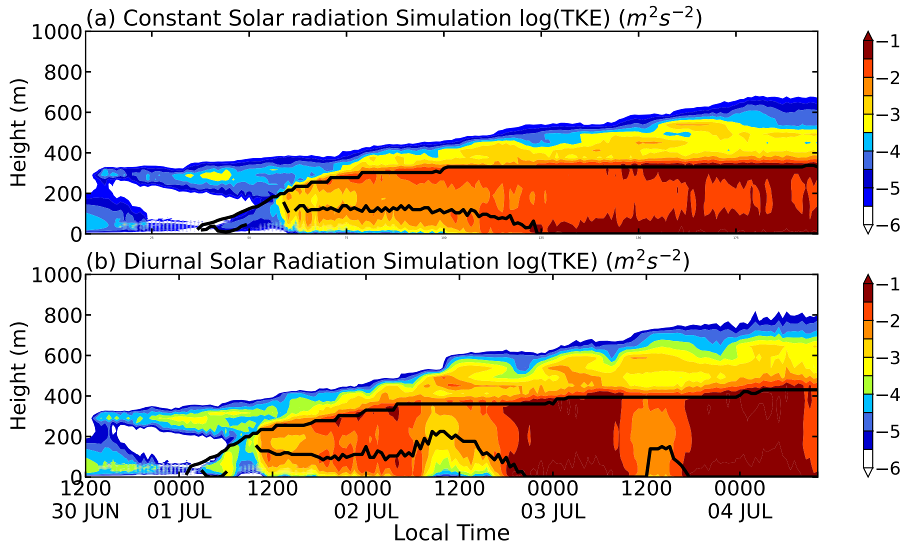

FIG. 10 Time-height section of $\log_{10}$(TKE) (shading in $m^2\ s^{-2}$), and time series of fog/cloud top height (upper black lines in m) and thermal turbulence interface (lower black lines in m) for the simulations with constant (a) and diurnal (b) solar radiations.

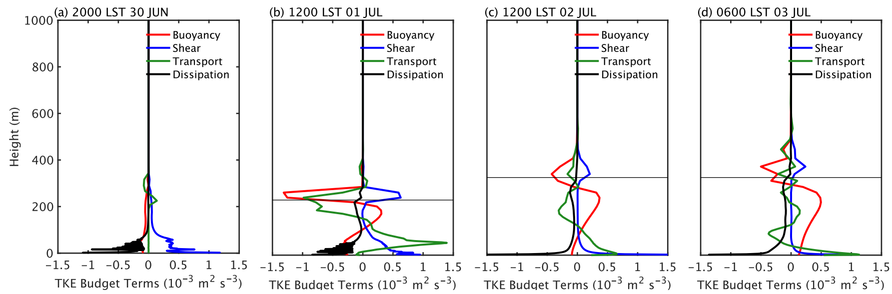

FIG. 11 Profiles of horizontal mean TKE budget terms ($10^{-3}\ m^2\ s^{-3}$) for the constant solar radiation simulation at (a) 2000 LST on 30, (b) 1200 LST on 01 July, (c) 1200 on 02 July and (d) 0600 LST on 03 July. Thin black lines indicate fog/cloud tops.

The turbulence in the ssC fog intensifies after its formation at 1200 LST on 02 July (Fig. 10a). However, the terms in the TKE budget exhibit a general weakening trend from fog formation to the ssC fog (Fig. 11c), possibly due to the reduced q_l gradient near the top of the fog layer (Fig. 6c). TKE exhibits a significant increase from the ssC fog to ssH fog, particularly near the surface. This is because the air-sea interface becomes unstable (SAT-SST < 0), leading to the buoyancy production of turbulence

https://doi.org/10.5194/egusphere-2023-1494
Preprint. Discussion started: 11 September 2023

(Fig. 11d). During this period, both buoyancy-induced and mechanically-induced turbulence contribute significantly to the maximum TKE near the surface.

The vertical structure of turbulence can be elucidated by employing the thermal turbulence interface, which distinguishes between the layers characterized by thermal and mechanical turbulence (Huang et al., 2015). The thermal turbulence interface is defined as the lowest altitude within the fog layer where the buoyancy production of turbulence is positive (the black lines in Fig. 10). Following the formation of fog, a thermal-turbulence mixing layer forms beneath the fog top and extends across the upper half of the fog layer from 0000 LST on 02 July (Fig. 10a). After 1200 LST on 02 July, the mixing layer continues to develop downward, eventually reaching the sea surface by 2200 LST on the same day, thus establishing a well-mixed boundary layer. Subsequently, the thermal turbulence cools the near-surface air and causes SAT to drop below SST after a 2-hour interval (Fig. 5b).

5 Simulation with diurnal solar radiation

We conduct an additional simulation that incorporates diurnal solar radiation. Overall, the simulated fog with diurnal solar radiation exhibits similar behavior to that in the simulation with constant solar radiation, but with clear diurnal variations. Fog forms at 0200 LST on 01 July, followed by a brief transition into stratus at 1600 LST on 02 July (Fig. 12a). Within 1 hour, the cloud base height rapidly rises to 80 m, but then decreases due to the weakening and disappearance of solar radiation. Subsequently, fog reoccurs at 2000 LST and eventually transitions into stratus at 0900 LST on 03 July.

The simulation incorporating diurnal solar radiation also generates ssH fog, which exhibits significant diurnal variation. During the nights of 03 July and 04 July, SAT rapidly drops below SST after sunset and recovers above SST after sunrise. Surprisingly, the UCLA-LES successfully simulates the diurnal variation in SAT-SST during the advection fog episode, indicating that the diurnal variation in the radiative balance over the fog top considerably alters the transitions between ssC and ssH fog (Fig. 2b). Additionally, both TKE and the thermal-turbulence mixing layer exhibit distinct diurnal variations. The pronounced radiative cooling at the fog top results in increased TKE

https://doi.org/10.5194/egusphere-2023-1494
Preprint. Discussion started: 11 September 2023

and a thicker thermal-turbulence mixing layer at nighttime compared to daytime (Fig. 10b).

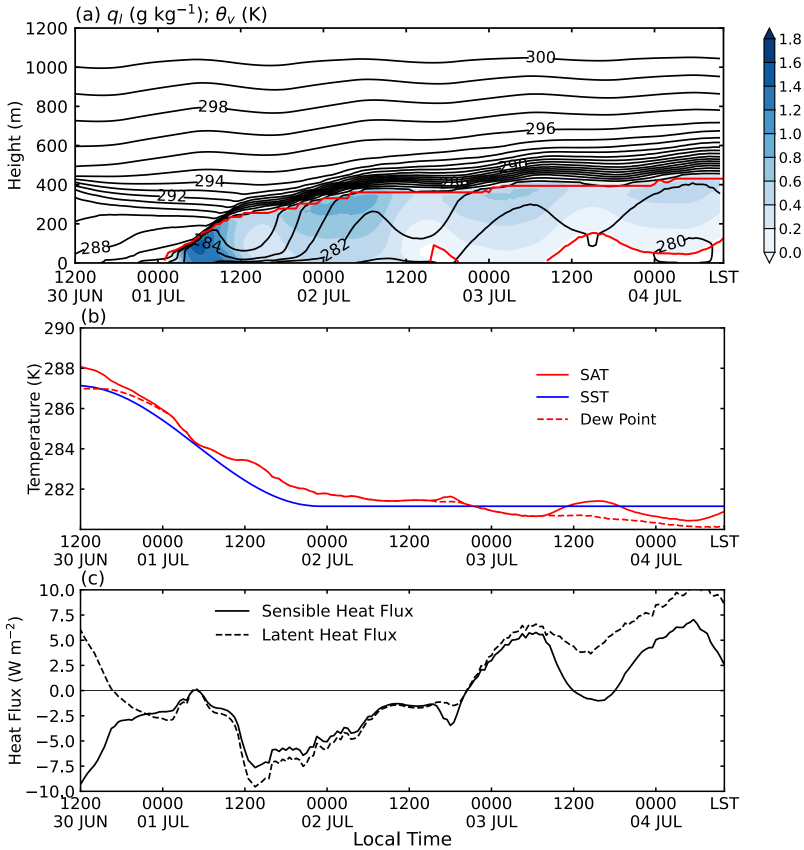

FIG. 12 As in Fig. 5, but for the simulation with diurnal cycle radiation.

6 Summary and discussion

Sea fog is of great importance due to its significant impact on maritime activities. The present study synthesizes the long-term shipborne observations and a LES model to explore the phenomena of negative SAT-SST during advection fog over the NWP (referred to ssH fog). The UCLA-LES successfully simulates a fog event with ssH fog and captures the diurnal variation in SAT-SST during the fog episode. The simulation results highlight the strong influence of the LWC effect at the fog top on the formation of ssH fog.

Long-term shipborne observations reveal the prevalence of advection fog along the cold flank of the SST front in the NWP during the boreal summer. The ssH fog often occurs downstream of the regime of the advection fog with positive SAT-SST. The relative frequency ssH during episodes of advection fog is ~27.5% in JJA, which is roughly consistent with the results over the summertime Yellow Sea (Yang et al. 2021) and wintertime northeast Pacific (Li et al. 2022). Furthermore, our findings reveal, for the first time, that the relative frequency of ssH fog exhibits a distinct diurnal cycle, with a peak occurrence (~34.5%) before sunrise and a trough occurrence (~18.8%) in the afternoon (Fig. 2b). This suggests that the thermal dynamics and associated turbulence structure of advection fog exhibit significant diurnal variation.

From a Lagrangian perspective, we utilize the turbulence-closure UCLA-LES model to simulate an advection fog event over the NWP from 01 to 04 July 2013, which exhibits similar characteristics to the long-term features of ssH fog. Surprisingly, the LES model successfully reproduces the diurnal variation in SAT-SST during the fog episode when incorporating diurnal solar radiation (Fig. 12), indicating that the model captures the essential processes responsible for ssH fog.

We detailed analyze the LES simulation with constant solar radiation, which also produces ssH fog during the advection fog episode. Before the fog formation, the decreased SST over the oceanic front cools the near-surface air through the mechanical turbulence and triggers fog occurrence. Around the fog initiation, the cold sea surface drives a stable layer below 40 m in altitude, which decouples the fog layer from the sea surface. Once the surface vapor condenses, in the perspective of the fog layer, the fog-top LWC effect rapidly exceeds the near-surface mechanical cooling within ~2 hours after the fog formation (Fig. 9), when the air colume is still on the SST front. A thermal turbulence interface, separating the layers characterized by thermal and mechanical turbulence, well depicts the evolution of the vertical turbulence structure (Fig. 10a). The thermal turbulence from the fog top gradually develops downward to transport the fog-top LWC effect and reaches the surface 43 hours after the fog formation.

Our LES results indicate that ssH fog occurs when the thermal turbulent layer generated by the LWC at the fog top extends throughout the entire fog layer, causing the near-surface air to cool below the sea surface temperature (SST). Previous studies

https://doi.org/10.5194/egusphere-2023-1494
Preprint. Discussion started: 11 September 2023

have primarily focused on the near-surface liquid water in sea fog to validate the performance of models in simulating sea fog (e.g., Gao et al. 2007; Yang et al. 2018; 2019). Considering the limited availability of observations on the vertical structure of fog over the open sea (e.g., Huang et al. 2015), the occurrence of ssH fog during advection fog episodes provides valuable additional observations for improving the modeling of the thermal turbulence induced by the LWC at the fog top.

The comparison with the results from Yang et al. (2021) demonstrates that increased descending motion plays a significant role in intensifying the cooling of the fog layer by enhancing the LWC at the fog top. Moreover, stronger descending motion leads to longer fog duration and lower fog top height. These findings indicate that large-scale descending motion modulates the characteristics of fog by altering the LWC at the fog top.

Acknowledgments. This work is supported by the National Key Research and Development Program of China (2018YFA0605700), and the Natural Science Foundation of China (41875012). L. Y. are supported by the National Key R&D Program of China (2021YFB2601701), and S. D. are supported by Natural Science Foundation of Shandong Province (ZR2019ZD12).

Open Research

Data Availability Statement

The data used in this study are obtained from the ECMWF which is available at https://www.ecmwf.int/en/forecasts/datasets/reanalysis-datasets/era5 and the ICOADS data at https://icoads.noaa.gov/.

Competing interests

The contact author has declared that neither they nor their co-authors have any competing interests.

https://doi.org/10.5194/egusphere-2023-1494
Preprint. Discussion started: 11 September 2023

Reference

Bari, D., Bergot, T., and El Khlifi, M.: Local Meteorological and Large-Scale Weather Characteristics of Fog over the Grand Casablanca Region, Morocco, J. Appl. Meteorol. Climatol., 55, 1731–1745, https://doi.org/10.1175/JAMC-D-15-0314.1, 2016.

Bergot, T.: Small-scale structure of radiation fog: A large-eddy simulation study, Q. J. R. Meteorol. Soc., 139, 1099–1112, https://doi.org/10.1002/QJ.2051, 2013.

Bretherton, C. S. and Wyant, M.: Moisture transport , lower-tropospheric stability , and Decoupling of cloud-topped boundary layers, J. Atmos. Sci., 148–167, 1997.

Douglas, C.: Cold fogs over the sea, Meteor. Mag, 65, 133–135, 1930.

Findlater, J., Roach, W. T., and McHugh, B. C.: The haar of north-east Scotland, Q. J. R. Meteorol. Soc., 115, 581–608, https://doi.org/10.1002/qj.49711548709, 1989.

Fu, G. and Song, Y.: Climatic characteristics of sea fog frequency over the North Pacific Ocean, Period. Ocean Univ. China, 44, 35–41, 2014.

Fu, Q. and Liou, K. N.: Parameterization of the Radiative Properties of Cirrus Clouds, J. Atmos. Sci., 50, 2008–2025, https://doi.org/10.1175/1520-0469(1993)050, 1993.

Gao, S., Lin, H., Shen, B., and Fu, G.: A heavy sea fog event over the Yellow Sea in March 2005: Analysis and numerical modeling, Adv. Atmos. Sci., 24, 65–81, https://doi.org/10.1007/s00376-007-0065-2, 2007.

Gerber, H., Frick, G., Malinowski, S. P., Brenguier, J. L., and Burnet, F.: Holes and Entrainment in Stratocumulus, J. Atmos. Sci., 62, 443–459, https://doi.org/10.1175/JAS-3399.1, 2005.

Gerber, H., Frick, G., Malinowski, S. P., Jonsson, H., Khelif, D., and Krueger, S. K.: Entrainment rates and microphysics in POST stratocumulus, J. Geophys. Res. Atmos., 118, 12,094-12,109, https://doi.org/10.1002/JGRD.50878, 2013.

Guan, H., Yau, M. K., and Davies, R.: The Effects of Longwave Radiation in a Small Cumulus Cloud, J. Atmos. Sci., 54, 2201–2214, https://doi.org/10.1175/1520-0469(1997)054, 1997.

Gultepe, I., Tardif, R., Michaelides, S. C., Cermak, J., Bott, A., Bendix, J., Müller, M.

https://doi.org/10.5194/egusphere-2023-1494
Preprint. Discussion started: 11 September 2023

D., Pagowski, M., Hansen, B., Ellrod, G., Jacobs, W., Toth, G., and Cober, S. G.: Fog research: A review of past achievements and future perspectives, Pure Appl. Geophys., 164, 1121–1159, https://doi.org/10.1007/s00024-007-0211-x, 2007.

Hersbach, H., Bell, B., Berrisford, P., Hirahara, S., Horányi, A., Muñoz-Sabater, J., Nicolas, J., Peubey, C., Radu, R., Schepers, D., Simmons, A., Soci, C., Abdalla, S., Abellan, X., Balsamo, G., Bechtold, P., Biavati, G., Bidlot, J., Bonavita, M., De Chiara, G., Dahlgren, P., Dee, D., Diamantakis, M., Dragani, R., Flemming, J., Forbes, R., Fuentes, M., Geer, A., Haimberger, L., Healy, S., Hogan, R. J., Hólm, E., Janisková, M., Keeley, S., Laloyaux, P., Lopez, P., Lupu, C., Radnoti, G., de Rosnay, P., Rozum, I., Vamborg, F., Villaume, S., and Thépaut, J. N.: The ERA5 global reanalysis, Q. J. R. Meteorol. Soc., 146, 1999–2049, https://doi.org/10.1002/QJ.3803, 2020.

Hu, R., Dong, K., and Zhou, F.: Numerical experiments with the advection, turbulence and radiation effects in the seafog formation process, Adv. Mar. Sci., 24, 156, 2006.

Huang, H., Liu, H., Huang, J., Mao, W., and Bi, X.: Atmospheric boundary layer structure and turbulence during sea fog on the southern China coast, Mon. Weather Rev., 143, 1907–1923, https://doi.org/10.1175/MWR-D-14-00207.1, 2015.

Jiang, H., Xue, H., Teller, A., Feingold, G., and Levin, Z.: Aerosol effects on the lifetime of shallow cumulus, Geophys. Res. Lett., 33, https://doi.org/10.1029/2006GL026024, 2006.

Koračin, D. and Dorman, C. (Eds.): Marine fog: Challenges and advancements in observations, modeling, and forecasting, Springer Atmospheric Sciences, 537 pp., 2017.

Koračin, D., Lewis, J., Thompson, W. T., Dorman, C. E., and Businger, J. A.: Transition of stratus into fog along the California coast: Observations and modeling, J. Atmos. Sci., 58, 1714–1731, https://doi.org/10.1175/1520-0469(2001)058<1714:TOSIFA>2.0.CO;2, 2001.

Kunkel, B. A.: Parameterization of droplet terminal velocity and extinction coefficient in fog models, J. Appl. Meteorol. Climatol., 23, 34–41, 1984.

Lamb, H.: Haars or North Sea fogs on the coasts of Great Britain, Meteorol. Off. Publl.

https://doi.org/10.5194/egusphere-2023-1494
Preprint. Discussion started: 11 September 2023

MO, 504, 24, 1943.

Leipper, D. F.: Fog development at San Diego, California, 1948.

Leipper, D. F.: Fog on the U.S. West Coast: A Review, https://doi.org/10.1175/1520-0477(1994)075<0229:FOTUWC>2.0.CO;2, 1994.

Leipper, D. F. and Lewis, J. M.: Modeling sea fog on the U . S . California coast during a hot spell event, 22, 2005.

Lewis, J. M., Koračin, D., and Redmond, K. T.: Sea fog research in the United Kingdom and United States. A historical essay including outlook, Bull. Am. Meteorol. Soc., 85, 395–408, https://doi.org/10.1175/BAMS-85-3-395, 2004.

Li, X., Zhang, S., Koračin, D., Yi, L., and Zhang, X.: Atmospheric conditions conducive to marine fog over the northeast Pacific in winters of 1979–2019, Front. Earth Sci., 10, 942846, https://doi.org/10.3389/FEART.2022.942846/BIBTEX, 2022.

Lilly, D. K.: The representation of small-scale turbulence in numerical simulation experiments, in: Proc. IBM Sci. Comput. Symp. on Environmental Science, 195–210, 1967.

Long, J., Zhang, S., Chen, Y., Liu, J., and Han, G.: Impact of the Pacific–Japan teleconnection pattern on July sea fog over the northwestern Pacific: Interannual variations and global warming effect, Adv. Atmos. Sci., 33, 511–521, https://doi.org/10.1007/s00376-015-5097-4, 2016.

Maronga, B. and Reuder, J.: On the Formulation and Universality of Monin–Obukhov Similarity Functions for Mean Gradients and Standard Deviations in the Unstable Surface Layer: Results from Surface-Layer-Resolving Large-Eddy Simulations, J. Atmos. Sci., 74, 989–1010, https://doi.org/10.1175/JAS-D-16-0186.1, 2017.

McGibbon, J. and Bretherton, C. S.: Skill of ship-following large-eddy simulations in reproducing MAGIC observations across the northeast Pacific stratocumulus to cumulus transition region, J. Adv. Model. Earth Syst., 9, 810–831, https://doi.org/10.1002/2017MS000924, 2017.

Nakanishi, M.: Large-eddy simulation of radiation fog, Boundary-Layer Meteorol., 94, 461–493, https://doi.org/10.1023/A:1002490423389/METRICS, 2000.

Petterssen, S.: On the Causes and the Forecasting of the California Fog, Bull. Am.

Meteorol. Soc., 19, 49–55, https://doi.org/10.1175/1520-0477-19.2.49, 1938.

Pincus, R. and Stevens, B.: Monte Carlo Spectral Integration: a Consistent Approximation for Radiative Transfer in Large Eddy Simulations, J. Adv. Model. Earth Syst., 1, n/a-n/a, https://doi.org/10.3894/JAMES.2009.1.1, 2009.

Pincus, R., Baker, M. B., and Bretherton, C. S.: What Controls Stratocumulus Radiative Properties? Lagrangian Observations of Cloud Evolution, J. Atmos. Sci., 54, 2215–2236, https://doi.org/10.1175/1520-0469(1997)054, 1997.

RODHE, B.: The effect of turbulence on fog formation, Tellus, 14, 49–86, https://doi.org/10.1111/J.2153-3490.1962.TB00119.X, 1962.

Rogers, D. P. and Koračin, D.: Radiative transfer and turbulence in the cloud-topped marine atmospheric boundary layer, J. Atmos. Sci., 49, 1473–1486, 1992.

Savic-Jovcic, V. and Stevens, B.: The Structure and Mesoscale Organization of Precipitating Stratocumulus, J. Atmos. Sci., 65, 1587–1605, https://doi.org/10.1175/2007JAS2456.1, 2008.

Schwenkel, J. and Maronga, B.: Large-eddy simulation of radiation fog with comprehensive two-moment bulk microphysics: Impact of different aerosol activation and condensation parameterizations, Atmos. Chem. Phys., 19, 7165–7181, https://doi.org/10.5194/ACP-19-7165-2019, 2019.

Seifert, A. and Beheng, K. D.: A double-moment parameterization for simulating autoconversion, accretion and selfcollection, Atmos. Res., 59–60, 265–281, https://doi.org/10.1016/S0169-8095(01)00126-0, 2001.

Smagorinsky, J.: General circulation experiments with the primitive equations: I. The basic experiment, Mon. Weather Rev., 91, 99–164, 1963.

Stevens, B.: Cloud transitions and decoupling in shear-free stratocumulus-topped boundary layers, Geophys. Res. Lett., 27, 2557–2560, https://doi.org/10.1029/1999GL011257, 2000.

Stevens, B., Lenschow, D. H., Faloona, I., Moeng, C. H., Lilly, D. K., Blomquist, B., Vali, G., Bandy, A., Campos, T., Gerber, H., Haimov, S., Morley, B., and Thornton, D.: On entrainment rates in nocturnal marine stratocumulus, Q. J. R. Meteorol. Soc., 129, 3469–3493, https://doi.org/10.1256/QJ.02.202, 2003.

Stevens, B., Moeng, C. H., Ackerman, A. S., Bretherton, C. S., Chlond, A., de Roode, S., Edwards, J., Golaz, J. C., Jiang, H., Khairoutdinov, M., Kirkpatrick, M. P., Lewellen, D. C., Lock, A., Müller, F., Stevens, D. E., Whelan, E., and Zhu, P.: Evaluation of Large-Eddy Simulations via Observations of Nocturnal Marine Stratocumulus, Mon. Weather Rev., 133, 1443–1462, https://doi.org/10.1175/MWR2930.1, 2005.

Taylor, G. I.: The formation of fog and mist, Q. J. R. Meteorol. Soc., 43, 241–268, https://doi.org/10.1002/qj.49704318302, 1917.

Tokinaga, H. and Xie, S.-P.: Ocean tidal cooling effect on summer sea fog over the Okhotsk Sea, J. Geophys. Res., 114, D14102, https://doi.org/10.1029/2008JD011477, 2009.

Tremant, M.: La prévision du brouillard en mer. Météorologie Maritime et Activities Océanographique Connexes, Rapport No. 20. TD no. 211, World Meteorol. Organ. Geneva, Switz., 1987.

Wainwright, C. and Richter, D.: Investigating the Sensitivity of Marine Fog to Physical and Microphysical Processes Using Large-Eddy Simulation, 181, 473–498, https://doi.org/10.1007/s10546-020-00599-6, 2021.

Wang, B.: Sea fog, China Ocean Press, Beijing, 352 pp., 1983.

Wyant, M. C., Bretherton, C. S., Rand, H. A., and Stevens, D. E.: Numerical simulations and a conceptual model of the stratocumulus to trade cumulus transition, http://journals.ametsoc.org/doi/abs/10.1175/1520-0469(1997)054%3C0168:NSAACM%3E2.0.CO;2, 1997.

Yamaguchi, T. and Randall, D. A.: Large-Eddy Simulation of Evaporatively Driven Entrainment in Cloud-Topped Mixed Layers, J. Atmos. Sci., 65, 1481–1504, https://doi.org/10.1175/2007JAS2438.1, 2008.

Yang, L., Liu, J. W., Ren, Z. P., Xie, S. P., Zhang, S. P., and Gao, S. H.: Atmospheric conditions for advection-radiation fog over the western Yellow Sea, J. Geophys. Res. Atmos., 123, 5455–5468, https://doi.org/10.1029/2017JD028088, 2018.

Yang, L., Liu, J.-W., Xie, S.-P., and Shen, S. S. P.: Transition from Fog to Stratus over the Northwest Pacific Ocean: Large-eddy Simulation, Mon. Weather Rev., 2913–

2925, https://doi.org/10.1175/mwr-d-20-0420.1, 2021.

Yang, Y. and Gao, S.: The Impact of turbulent diffusion driven by fog-top cooling on sea fog Development, J. Geophys. Res. Atmos., https://doi.org/10.1029/2019JD031562, 2020.

Yang, Y., Hu, X. M., Gao, S., and Wang, Y.: Sensitivity of WRF simulations with the YSU PBL scheme to the lowest model level height for a sea fog event over the Yellow Sea, Atmos. Res., https://doi.org/10.1016/j.atmosres.2018.09.004, 2019.

Zhang, S., Li, M., Meng, X., Fu, G., Ren, Z., and Gao, S.: A comparison study between spring and summer fogs in the Yellow Sea-observations and mechanisms, Pure Appl. Geophys., 169, 1001–1017, https://doi.org/10.1007/s00024-011-0358-3, 2012.

Zhang, S., Chen, Y., Long, J., and Han, G.: Interannual variability of sea fog frequency in the Northwestern Pacific in July, Atmos. Res., 151, 189–199, https://doi.org/10.1016/j.atmosres.2014.04.004, 2015.

Zhang, S. P. and Ren, Z. P.: The influence of thermal effects of underlaying surface on the spring sea fog over the Yellow Sea—Observations and numerical simulation, Acta Meteorol. Sin., 68, 439–449, 2010.